Performance Calculation for Single-Sided Linear Induction Motors with a Double-Layer Reaction Rail Under Constant Current Excitation

JACEK F. GIERAS, MEMBER, IEEE, GRAHAM E. DAWSON, MEMBER, IEEE, AND ANTHONY R. EASTHAM, SENIOR MEMBER, IEEE

Abstract—**A method for computing the performance of a single-sided linear induction motor (SLIM) with a double-layer reaction rail, under constant current excitation, is presented. This method takes into account the reaction of secondary eddy currents on the airgap field, transverse edge and longitudinal end effects, together with skin effect, saturation, nonlinear magnetic permeability, and hysteresis in the solid steel core of a reaction rail. In an equivalent circuit of the machine, the mutual and secondary impedances are found from a solution of the two-dimensional electromagnetic field distribution. Modifying factors account for configurations in which the width of the secondary conductive layer is different from that of the steel core, and in which the thickness of the conductive overhand is different from that over the steel core. Good correlation is obtained between analysis and test results from a large-scale linear induction motor (LIM) at Queen's University. The developed expressions are appropriate for small and large LIM's and may also be used for constant voltage excitation conditions.**

INTRODUCTION

THE SINGLE-SIDED linear induction motor (SLIM) provides both wheeled and noncontact vehicles with a low maintenance adhesion-free means of propulsion and braking [1]–[5]. As further applications for SLIM's are examined, there will be a growing need for analytical tools which will not only accurately predict the performance of a machine of given design but which will allow the computer-aided design of a machine to a given set of specifications. The SLIM with a solid steel reaction rail fed from a constant current source has already been analyzed by the authors [6]. Comparative tests [7] have shown that a secondary consisting of a conductive (usually aluminum) cap over laminated (or solid) steel core produces the greatest thrust with the highest efficiency-power factor ($\eta \cos \phi$) product and with the lowest normal force. This reaction rail is, therefore, favored for noncontact traction purposes.

The purpose of this paper is to present a versatile method for calculating the performance of a SLIM with an aluminum-capped reaction rail. This configuration is analogous to that in a rotating induction motor with double-layer rotor [8]–[10]. Although many analyses for linear induction machines with layered secondaries have been published [2], [11]–[16], the methods are not always appropriate for design studies of transportation SLIM's. Analytical results are usually not close to measured values over a wide range of operating conditions because of neglected or inadequate treatment of skin, edge and end effects, magnetic saturation, and hysteresis. Commonly used correction factors are not sufficiently accurate at high levels of excitation when parts of the magnetic circuit are driven into saturation.

In this paper we show that the performance of a SLIM can be evaluated from an equivalent circuit which is very similar to that commonly used for the rotating machine. Mutual and secondary parameters are derived from an evaluation of the two-dimensional field in a longitudinal section of the machine, and are speed and slip frequency dependent. Generally applicable and validated correction factors are presented to account for the finite length and width of the machine and for the geometry and electromagnetic properties of the reaction rail.

ANALYTICAL APPROACH

From a computational point of view, the calculation of the two-dimensional field in a longitudinal section of a SLIM is preferable to a full three-dimensional analysis and is entirely adequate for SLIM performance evaluation. In this way we avoid double Fourier series and space harmonics along the primary slots (in the y direction). In two-dimensional analysis the currents flow only in the y direction, and the magnetic flux density has only two components; perpendicular B_{mz} and parallel B_{mx} to the direction of motion (x direction). A section of the machine to be analyzed is shown in Fig. 1.

The double-layer reaction rail of a SLIM comprises an aluminum cap over laminated or solid steel core. The core serves to carry the airgap flux and to reduce the magnetizing current of the machine. Lamination of the core, as opposed to the use of solid steel, improves the performance, particularly for low-speed running. However lamination is expensive and is not cost effective for sections of the guideway in which a LIM is operated at intermediate or high speed due to end effects [17].

When the secondary core is formed from solid material, this layer will also carry slip frequency induced currents.

Manuscript received September 12, 1984; revised May 24, 1985. This work was supported by the Natural Sciences and Engineering Research Council (NSERC) of Canada.

The authors are with the Department of Electrical Engineering, Queen's University, Kingston, Ontario, Canada K7L 3N6.

0018-9464/86/0100-0054$1.00 © 1986 IEEE

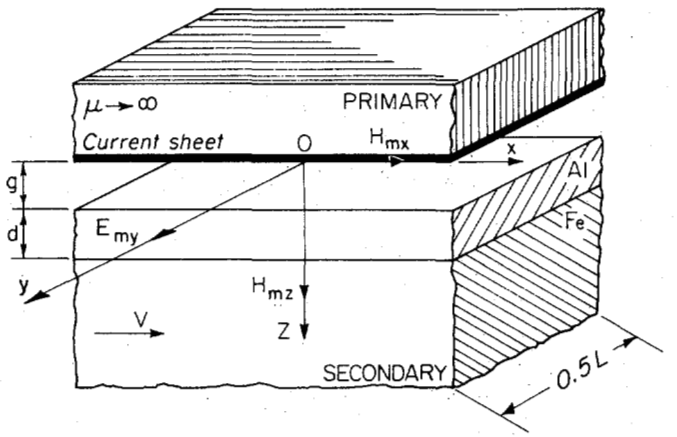

Fig. 1. Model of single-sided linear induction motor with double-layer secondary.

The effective secondary resistance now becomes smaller than for a laminated core. In addition the magnetic properties of cast steel are such that variable permeability and hysteresis losses of the core will have a significant effect on the secondary impedance. These effects should be included in any general model for SLIM design and analysis.

The analysis of a SLIM with double layer secondary presented here includes

1) skin effect in the secondary,
2) reaction of the secondary eddy current on the primary magnetic field,
3) saturation and hysteresis effects in the solid core of the secondary,
4) longitudinal end and transverse edge effects.

The two-dimensional electromagnetic field distribution is described by equations in series form which take into account the skin effect and reaction of the secondary eddy current. Saturation and hysteresis effects are included by means of the equivalent relative magnetic permeability of solid steel, μ_{re} [18]:

$$\mu_{re} = \mu_{rs}(\mu' - j\mu'') \tag{1}$$

where μ_{rs} is the surface value of relative magnetic permeability. The real and imaginary components, μ' and μ'', are described in [18].

The saturation factor for the magnetic circuit (see Appendix I) is given by

$$k_\mu = \frac{V}{2(V_g + V_d)} \tag{2}$$

where V equals the magnetomotive force (MMF) per pole pair, V_g is the magnetic potential drop across the airgap, and V_d is the magnetic potential drop across the nonmagnetic layer (i.e., the aluminum cap). In accordance with classical theory of electrical machines, the saturation factor influences the magnetizing reactance (discussed later), and the differential and slot leakage reactances of the primary.

Carter's coefficient k_c is used to obtain the equivalent airgap of the machine:

$$g' = k_c g. \tag{3}$$

The Carter coefficient must be calculated for the entrefer $(g + d)$, and it should be noted that the slot opening of the primary may have a lower magnitude than $(g + d)$.

Transverse edge effect in the solid steel reaction plate is included by correction factors described in the paper [6]. Russell and Norsworthy's correction factor [19] is used for edge effect in the high conductivity nonmagnetic layer (see Appendix II). The corrected conductivity of the aluminum cap is then

$$\sigma'_{Al} = \sigma_{Al} k_{RN}. \tag{4}$$

There are four methods for taking longitudinal end effect into account:

1) by superposition of traveling and pulsating fields [20],
2) by superposition of a wave traveling at synchronous speed and two end-effect waves [3],
3) by postulating a periodic distribution of SLIM's, and representing the resultant space harmonics by Fourier series [14], [21],
4) by modifying the electromotive force (EMF) across the mutual impedance of a T-type equivalent circuit [22], [27].

The last technique is considered to give the best results and is the simplest analytically and computationally. The end effect factor is defined as [27]

$$k_e = \frac{E_{me}}{E_{ms}} \tag{5}$$

where E_{ms} is the peak value of the EMF induced in a primary phase winding by the magnetic flux density wave traveling with synchronous velocity, and E_{me} is the peak value of EMF induced by the damped entry-end wave [3]. This method is used in this paper to compute the performance of SLIM's with double-layer secondaries, under constant current excitation.

Equations of Electromagnetic Field Distribution

Development of the electromagnetic field equations allows the secondary and mutual impedances in the equivalent circuit of the SLIM to be determined. The plane of electromagnetic field analysis consists of three isotropic layers; the first layer is steel halfspace, the second layer is aluminum or copper plate with thickness d, and the third layer is equivalent airgap g' (3).

The assumptions for the establishment of the electromagnetic field equations are as given in [6]. For the SLIM model with double-layer secondary, as shown in Fig. 1, the electromagnetic field equations are as follows.

1) For $0 \le z \le g'$

$$H_{mx3} = \sum_{\nu=1}^{\infty} \frac{1}{M_\nu} \left\{ \frac{\kappa_{\nu 2}}{\beta_\nu} \left[\frac{\kappa_{\nu 1}}{\kappa_{\nu 2}} \cosh(\kappa_{\nu 2} d) + \mu_{re} \sinh(\kappa_{\nu 2} d) \right] \cosh[\beta_\nu (z - g')] - \left[\mu_{re} \cosh(\kappa_{\nu 2} d) + \frac{\kappa_{\nu 1}}{\kappa_{\nu 2}} \sinh(\kappa_{\nu 2} d) \right] \cdot \sinh[\beta_\nu (z - g')] \right\} [-(A_{m\nu}^{+} e^{-j\beta_\nu x} + A_{m\nu}^{-} e^{j\beta_\nu x})] \quad (6)$$

$$H_{mz3} = \sum_{\nu=1}^{\infty} \frac{1}{M_\nu} \left\{ \left[\mu_{re} \cosh(\kappa_{\nu 2} d) + \frac{\kappa_{\nu 1}}{\kappa_{\nu 2}} \sinh(\kappa_{\nu 2} d) \right] \cdot \cosh[\beta_\nu (z - g')] - \frac{\kappa_{\nu 2}}{\beta_\nu} \left[\frac{\kappa_{\nu 1}}{\kappa_{\nu 2}} \cosh(\kappa_{\nu 2} d) + \mu_{re} \sinh(\kappa_{\nu 2} d) \right] \sinh[\beta_\nu (z - g')] \right\} \cdot j(A_{m\nu}^{+} e^{-j\beta_\nu x} - A_{m\nu}^{-} e^{j\beta_\nu x}) \quad (7)$$

$$E_{my3} = \sum_{\nu=1}^{\infty} \frac{1}{M_\nu} \left\{ \left[\mu_{re} \cosh(\kappa_{\nu 2} d) + \frac{\kappa_{\nu 1}}{\kappa_{\nu 2}} \sinh(\kappa_{\nu 2} d) \right] \cdot \cosh[\beta_\nu (z - g')] - \frac{\kappa_{\nu 2}}{\beta_\nu} \left[\frac{\kappa_{\nu 1}}{\kappa_{\nu 2}} \cosh(\kappa_{\nu 2} d) + \mu_{re} \sinh(\kappa_{\nu 2} d) \right] \sinh[\beta_\nu (z - g')] \right\} \cdot \frac{j\omega\mu_0}{\beta_\nu} (A_{m\nu}^{+} e^{-j\beta_\nu x} + A_{m\nu}^{-} e^{j\beta_\nu x}). \quad (8)$$

2) For $g' < z < d + g'$

$$H_{mx2} = \sum_{\nu=1}^{\infty} \frac{1}{M_\nu} \frac{\kappa_{\nu 2}}{\beta_\nu} \left\{ \frac{\kappa_{\nu 1}}{\kappa_{\nu 2}} \cosh[\kappa_{\nu 2}(z - d - g')] - \mu_{re} \sinh[\kappa_{\nu 2}(z - d - g')] \right\} \cdot [-(A_{m\nu}^{+} e^{-j\beta_\nu x} + A_{m\nu}^{-} e^{j\beta_\nu x})] \quad (9)$$

$$H_{mz2} = \sum_{\nu=1}^{\infty} \frac{1}{M_\nu} \left\{ \mu_{re} \cosh[\kappa_{\nu 2}(z - d - g')] - \frac{\kappa_{\nu 1}}{\kappa_{\nu 2}} \sinh[\kappa_{\nu 2}(z - d - g')] \right\} \cdot j(A_{m\nu}^{+} e^{-j\beta_\nu x} - A_{m\nu}^{-} e^{j\beta_\nu x}) \quad (10)$$

$$E_{my2} = \sum_{\nu=1}^{\infty} \frac{1}{M_\nu} \left\{ \mu_{re} \cosh[\kappa_{\nu 2}(z - d - g')] - \frac{\kappa_{\nu 1}}{\kappa_{\nu 2}} \sinh[\kappa_{\nu 2}(z - d - g')] \right\} \cdot \frac{j\omega_\nu\mu_0}{\beta_\nu} (A_{m\nu}^{+} e^{-j\beta_\nu x} + A_{m\nu}^{-} e^{j\beta_\nu x}). \quad (11)$$

3) For $z \ge d + g'$

$$H_{mx1} = \sum_{\nu=1}^{\infty} \frac{1}{M_\nu} \frac{\kappa_{\nu 1}}{\beta_\nu} e^{-\kappa_{\nu 1}(z - d - g')} \cdot [-(A_{m\nu}^{+} e^{-j\beta_\nu x} + A_{m\nu}^{-} e^{j\beta_\nu x})] \quad (12)$$

$$H_{mz1} = \sum_{\nu=1}^{\infty} \frac{1}{M_\nu} e^{-\kappa_{\nu 1}(z - d - g')} \cdot j(A_{m\nu}^{+} e^{-j\beta_\nu x} - A_{m\nu}^{-} e^{j\beta_\nu x}) \quad (13)$$

$$E_{my1} = \sum_{\nu=1}^{\infty} \frac{1}{M_\nu} e^{-\kappa_{\nu 1}(z - d - g')} \frac{j\omega_\nu\mu_0\mu_{re}}{\beta_\nu} \cdot (A_{m\nu}^{+} e^{-j\beta_\nu x} + A_{m\nu}^{-} e^{j\beta_\nu x}) \quad (14)$$

where

$$M_\nu = \frac{\kappa_{\nu 2}}{\beta_\nu} \left[\frac{\kappa_{\nu 1}}{\kappa_{\nu 2}} \cosh(\kappa_{\nu 2} d) + \mu_{re} \sinh(\kappa_{\nu 2} d) \right] \cdot \cosh(\beta_\nu g') + \left[\mu_{re} \cosh(\kappa_{\nu 2} d) + \frac{\kappa_{\nu 1}}{\kappa_{\nu 2}} \cdot \sinh(\kappa_{\nu 2} d) \right] \sinh(\beta_\nu g') \quad (15)$$

$$\beta_\nu = \nu\pi/\tau \quad (16)$$

$$\kappa_{\nu 1} = \sqrt{\alpha_{\nu 1}^2 + \beta_\nu^2} = (a_{R\nu\mathrm{Fe}} + j a_{x\nu\mathrm{Fe}}) k_{\nu\mathrm{Fe}} \quad (17)$$

$$\kappa_{\nu 2} = \sqrt{\alpha_{\nu 2}^2 + \beta_\nu^2} = (a_{R\nu\mathrm{Al}} + j a_{x\nu\mathrm{Al}}) k_{\nu\mathrm{Al}} \quad (18)$$

$$a_{R\nu\mathrm{Fe}} = \mathrm{Re}[\kappa_{\nu 1}]/k_{\nu\mathrm{Fe}} \quad (19)$$

$$a_{x\nu\mathrm{Fe}} = \mathrm{Im}[\kappa_{\nu 1}]/k_{\nu\mathrm{Fe}} \quad (20)$$

$$a_{R\nu\mathrm{Al}} = \mathrm{Re}[\kappa_{\nu 2}]/k_{\nu\mathrm{Al}} \quad (21)$$

$$a_{x\nu\mathrm{Al}} = \mathrm{Im}[\kappa_{\nu 2}]/k_{\nu\mathrm{Al}}. \quad (22)$$

The propagation constants and attenuation factors are equal to

$$k_{\nu\mathrm{Fe}} = \sqrt{\omega_\nu \mu_0 \mu_{rs} \sigma_{\mathrm{Fe}}/2} \quad (23)$$

$$k_{\nu\mathrm{Al}} = \sqrt{\omega_\nu \mu_0 \sigma'_{\mathrm{Al}}/2} \quad (24)$$

$$\alpha_{\nu 1} = \sqrt{j\omega_\nu \mu_0 \mu_{re} \sigma_{\mathrm{Fe}}} \quad (25)$$

$$\alpha_{\nu 2} = \sqrt{j\omega_\nu \mu_0 \sigma'_{\mathrm{Al}}}. \quad (26)$$

Time factors $\exp(j\omega_\nu^{+})$ in $A_{m\nu}^{+}$, H_{mx}^{+}, H_{mz}^{+}, E_{my}^{+}, and $\exp(j\omega_\nu^{-})$ in $A_{m\nu}^{-}$, H_{mx}^{-}, H_{mz}^{-}, E_{my}^{-}, have been eliminated. The peak values of line current density of the primary A, angular frequencies ω, and slips s, are given by the following formulae.

1) For forward traveling fields:

$$A_{m\nu}^{+} = \frac{mNk_{w\nu}\sqrt{2}\, I}{p\tau} \exp\left[j(\nu - 1) \frac{m - 1}{m} \pi \right] \quad (27)$$

$$\omega_\nu^{+} = s_\nu^{+} \omega = 2\pi f s_\nu^{+} \quad (28)$$

$$s_\nu^{+} = 1 - \nu(1 - s). \quad (29)$$

2) For backward traveling fields:

$$A_{m\nu}^{-} = \frac{mNk_{w\nu}\sqrt{2}\,I}{p\tau}\exp\left[-j(\nu+1)\frac{m-1}{m}\pi\right] \quad (30)$$

$$\omega_{\nu}^{-} = s_{\nu}^{-}\omega = 2\pi f s_{\nu}^{-} \quad (31)$$

$$s_{\nu}^{-} = 1 + \nu(1-s). \quad (32)$$

where m is the number of phases, N is the number of primary turns per phase, $k_{w\nu}$ is the winding factor for the νth space harmonic, p is the number of pole pairs, τ is the pole pitch, I is the primary current, and $s = (v_s - v)/v_s$. For $\nu = km \pm 1$, where $k = 0, 1, 2, 3, \cdots$, $\exp[1 \pm (\nu \mp 1)(1 - 1/m)\pi] = 1$, and $A_{m\nu}^{+} = A_{m\nu}^{-} = A_{m\nu}$.

Secondary Impedance

Unit secondary impedance due to each νth space harmonic is given by the ratio of tangential electric and magnetic field components, as given by (8) and (10):

$$z_{y\nu} = \left.\frac{E_{my2\nu}}{H_{mx2\nu}}\right|_{z=g'} = z_{\nu 1}\cdot z_{\nu 12} \quad (33)$$

where $z_{\nu 1}$ is the unit impedance of the solid steel plate, and $z_{\nu 12}$ is the unit equivalent impedance of the high conductivity nonmagnetic layer, which is dependent on parameters of the solid steel reaction plate. To take into account transverse edge effect, impedance $z_{\nu 1}$ should be multiplied by the edge effect factor $k_{z\nu} > 1$ [6], and electric conductivity of the nonmagnetic layer should be multiplied by Russell and Norsworthy's factor $k_{RN\nu} < 1$ (Appendix II), i.e.,

$$z_{\nu 1} = -\frac{j\omega_{\nu}\mu_0\mu_{re}}{\kappa_{\nu 1}}k_{z\nu} \quad (34)$$

$$z_{\nu 12} = -\frac{-\frac{1}{z_{\nu 1}}\frac{j\omega_{\nu}\mu_0}{\kappa_{\nu 2}}\sinh(\kappa_{\nu 2}d) + \cosh(\kappa_{\nu 2}d)}{\cosh(\kappa_{\nu 2}d) - \frac{\kappa_{\nu 2}}{j\omega_{\nu}\mu_0}z_{\nu 1}\sinh(\kappa_{\nu 2}d)} \quad (35)$$

where

$$\kappa_{\nu 2} = (a_{R\nu \mathrm{Al}} + ja_{x\nu \mathrm{Al}})\sqrt{\omega_{\nu}\mu_0\sigma_{\mathrm{Al}}k_{\mathrm{RN}\nu}/2}.$$

For $z_{\nu 1} \to \infty$, (33)–(35) give unit impedance of the aluminum cap, i.e.,

$$z_{\nu 2} = \frac{-j\omega_{\nu}\mu_0}{\kappa_{\nu 2}}\frac{1}{\tanh(\kappa_{\nu 2}d_2)}. \quad (36)$$

Secondary impedance referred to the primary winding is then;

$$Z'_{\nu\mathrm{sec}} = R'_{\nu\mathrm{sec}} + jX'_{\nu\mathrm{sec}} = z_{\nu 1}z_{\nu 12}k_{\mathrm{tr}\nu}\nu\frac{L}{\tau} = \frac{z_{\nu 1}z_{\nu 2}}{z_{\nu 1}+z_{\nu 2}}k_{\mathrm{tr}\nu}\frac{\nu L}{\tau} \quad (37)$$

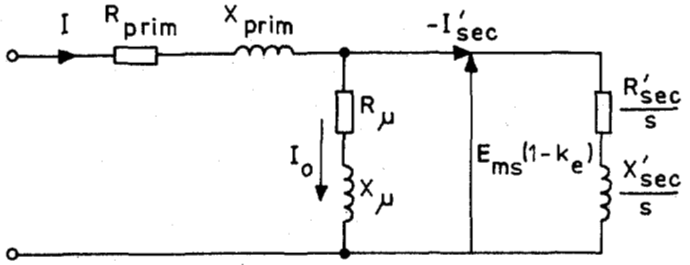

Fig. 2. Per phase equivalent circuit of linear induction motor.

where

$$k_{\mathrm{tr}\nu} = \frac{2m(Nk_{w\nu})^2}{\nu p}.$$

The impedance of the secondary branch of the T-type equivalent circuit, as shown in Fig. 2, can now be expressed as

$$\frac{Z'_{\nu\mathrm{sec}}}{s_{\nu}} = \frac{R'_{\nu\mathrm{sec}}}{s_{\nu}} + \frac{jX'_{\nu\mathrm{sec}}}{s_{\nu}} = \frac{z_{\nu 1}z_{\nu 2}}{z_{\nu 1}+z_{\nu 2}}k_{\mathrm{tr}\nu}\nu\frac{L}{\tau}\frac{1}{s_{\nu}}. \quad (38)$$

Mutual Impedance

Unit impedance "seen" below the primary current sheet can be calculated from (5) and (7), with $z = 0$, i.e.,

$$z_{\nu} = \left.\frac{E_{my3\nu}}{H_{mx3\nu}}\right|_{z=0} = z_{\nu 1}\cdot z_{\nu 12}\cdot z_{\nu 123} = z_{y\nu}\cdot z_{\nu 123} \quad (39)$$

where

$$z_{\nu 123} = \frac{-\frac{1}{z_{y\nu}}\frac{j\omega\mu_0}{\beta_{\nu}}\sinh(\beta_{\nu}g') + \frac{\omega}{\omega_{\nu}}\cosh(\beta_{\nu}g')}{\cosh(\beta_{\nu}g') - \frac{\omega}{\omega_{\nu}}\frac{\beta_{\nu}}{j\omega\mu_0}z_{y\nu}\sinh(\beta_{\nu}g')}. \quad (40)$$

If $z_{y\nu} \to \infty$, the unit reactance in the magnetizing branch can be obtained, i.e.,

$$z_{\nu 0} = -jx_{\nu 0} = -\frac{j\omega\mu_0}{\beta_{\nu}}\frac{1}{\tanh(\beta_{\nu}g')} \simeq -\frac{j\omega\mu_0}{\beta_{\nu}^2 g'}. \quad (41)$$

Magnetizing reactance referred to the primary winding is, therefore,

$$X_{\nu 0} = \frac{\omega\mu_0}{\beta_{\nu}^2 g'}k_{\mathrm{tr}\nu}\nu\frac{L_{\mathrm{prim}}}{\tau}. \quad (42)$$

To take into account active power losses in the primary core, an appropriate resistance $R_{\nu 0}$ should be connected in parallel with $X_{\nu 0}$. Mutual impedance, when resistance and reactance are connected in series, as in Fig. 2, is then given by

$$Z_{\nu\mu} = R_{\nu\mu} + jX_{\nu\mu} \quad (43)$$

where

$$R_{\nu\mu} = \frac{R_{\nu 0}X_{\nu 0}^2}{R_{\nu 0}^2 + X_{\nu 0}^2}$$

and

$$X_{\nu\mu} = \frac{R_{\nu 0}^2 X_{\nu 0}}{R_{\nu 0}^2 + X_{\nu 0}^2}. \tag{44}$$

To take into account saturation of the magnetic circuit, the airgap g' in (42) should be multiplied by the saturation factor k_μ, according to (3) and Appendix I, i.e., $g' = gk_c k_\mu$. The component of magnetizing current due to the nonmagnetic high conductivity layer is included in secondary impedance (37).

Thrust and Normal Force

Electromagnetic thrust for the fundamental space harmonic $\nu = 1$ is expressed by

$$F_x = \frac{m(I'_{\text{sec}})^2 R'_{\text{sec}}}{sv_s} \tag{45}$$

where R'_{sec} results from (37), and the secondary current referred to the primary winding is

$$I'_{\text{sec}} = \frac{E_{ms}(1 - k_e)}{\sqrt{\left(\frac{R'_{\text{sec}}}{s}\right)^2 + \left(\frac{X'_{\text{sec}}}{s}\right)^2}} \tag{46}$$

where k_e, the longitudinal end effect factor, is given by(5).

Normal force in the z direction consists of an attractive force F_{za}, and a repulsive eddy current reaction force F_{zr}, i.e.,

$$F_z = F_{za} - F_{zr}. \tag{47}$$

The attraction force is given by

$$F_{za} = \frac{1}{2\mu_0} B_{mzg}^2 p(\tau + \Delta x)L \tag{48}$$

where the normal component of magnetic flux density in the airgap is

$$B_{mzg} = \frac{E_{ms}(1 - k_e)}{4\sigma_k \alpha_i f N k_w \tau L}. \tag{49}$$

In (48), Δx represents an additional length due to half-filled end slots in the linear machine. Expressions for the form factor σ_k and for the ratio α_i of the average value to peak value of magnetic flux density are given in [6].

Because F_x is proportional to B_{mzg}, and F_{zr} is proportional to B_{mxg}, the eddy current reaction force is equal to

$$F_{zr} = F_x \frac{B_{mxg}}{B_{mzg}} \tag{50}$$

where F_x is expressed by formula (45), and the tangential component of magnetic flux density in the airgap may be found from (8) as

$$\begin{aligned} B_{mxg} &= \mu_0 \left| H_{mx2} \right|_{\nu=1, z=g', x=0} \\ &= \mu_0 \left| [\kappa_{\nu 1} \cosh(\kappa_{\nu 2} d) \right. \\ &\quad \left. + \kappa_{\nu 2} \mu_{re} \sinh(\kappa_{\nu 2} d)] \frac{-A_{m\nu}}{\beta_\nu M_\nu} \right|_{\nu=1}. \end{aligned} \tag{51}$$

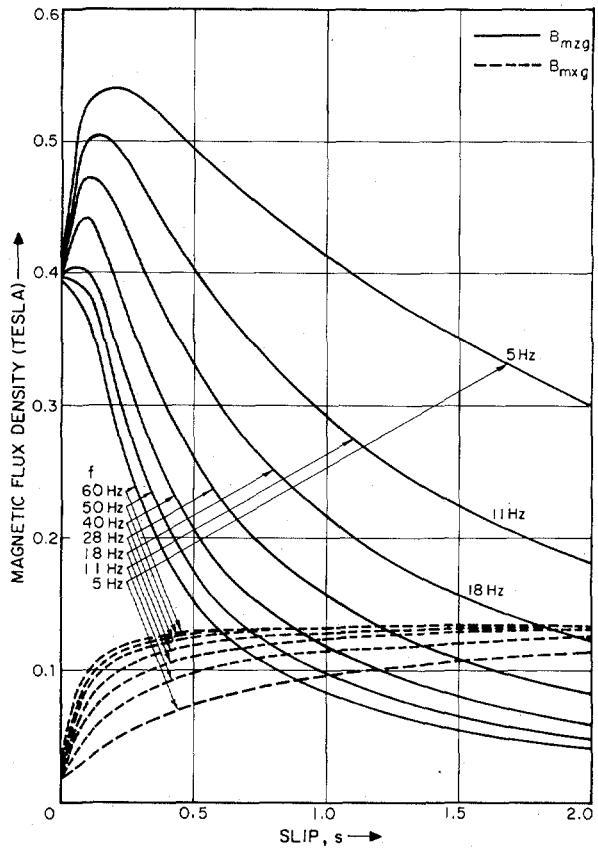

Fig. 3. Calculated peak values of normal and tangential components of magnetic flux density in airgap of the test LIM, at I = 200 A, g = 15 mm, d = 2.5 mm, w = 111 mm, h_{ov} = 33.9 mm.

Normal B_{mzg}, and tangential B_{mxg}, components of magnetic flux density for the test SLIM (see below) are plotted against slip in Fig. 3.

Comparison Between Analaysis and Test Results

The results computed from the analysis presented here were compared with experimental results obtained from a large-scale linear induction motor tested at Queen's University. The test facility consists of a 7.6-m diameter 0–101 km/h wheel, which carried the rim-mounted reaction rail, and a stationary LIM mounted in a six-component force balance and positional adjustment system. A PDP 11/03-based 64-channel data acquisition system accepts and processes test data corresponding to the phase voltages and currents (giving power and power factor), forces and moments with respect to the three coordinate axes, airgap and lateral offset at two positions along the LIM length, frequency, speed, and flux distribution in the machine. A complete description of the test facility and LIM equipment has been given previously [6], [7], [25].

The six-pole test LIM has a pole pitch of 0.25 m, a stack width of 0.101 m, and a 7/9 chorded winding [25]. The primary was excited by means of a 200-kVA variable-voltage variable-frequency inverter. The reaction rail consisted of a solid steel core, 111-mm wide by 25-mm deep, with an aluminum cap of thickness 2.5 mm over the core and 9.5 mm in the overhang.

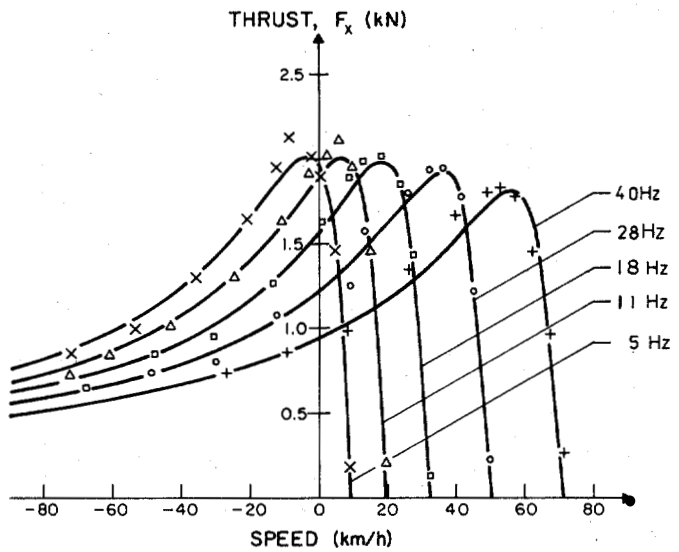

Fig. 4. Thrust F_x as function of speed at constant frequencies, for $I = 200$ A, $g = 15$ mm, $d = 2.5$ mm, $w = 111$ mm, $h_{ov} = 33.9$ mm.

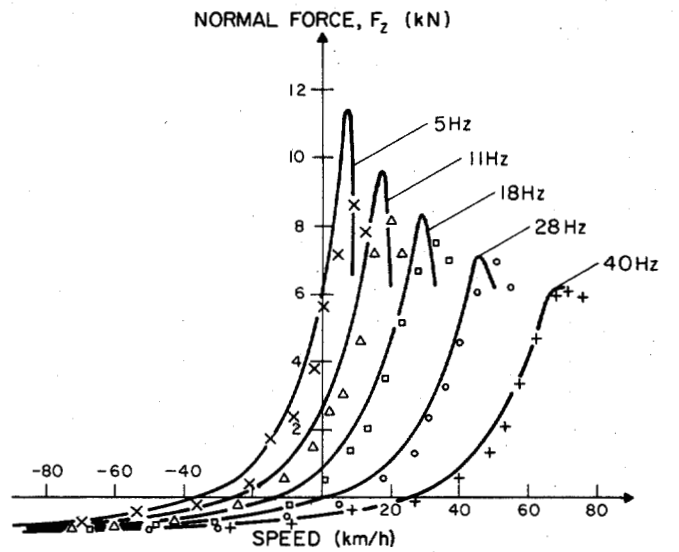

Fig. 5. Normal force F_z as a function of speed at constant frequencies, for $I = 200$ A, $g = 15$ mm, $d = 2.5$ mm, $w = 111$ mm, $h_{ov} = 33.9$ mm.

Computation of the performance of a LIM with double-layer secondary was performed in a similar way to that used for the LIM with solid steel secondary [6]. The test program was conducted over a range of speeds for various levels of constant current excitation, at discrete values of frequency and airgap. In order to evaluate the effect of aluminum cap rail overhang, tests were conducted as the width of this overhang was incrementally reduced to zero.

Figs. 4 and 5 compare analytical and test results for thrust and normal forces as a function of speed at various frequencies, for $I = 200$ A, $g = 15$ mm, and with a secondary overhang width $h_{ov} = 33.9$ mm.

The influence of aluminum cap overhang on thrust and normal forces at $I = 200$ A, $g = 15$ mm, $f = 18$ Hz is shown in Figs. 6 and 7. The method of taking the overhand dimension into account is described in Appendix II.

The effect of airgap on thrust and normal forces (at $I = 200$ A, $f = 18$ Hz, $h_{ov} = 33.9$ mm) is shown in Figs. 8

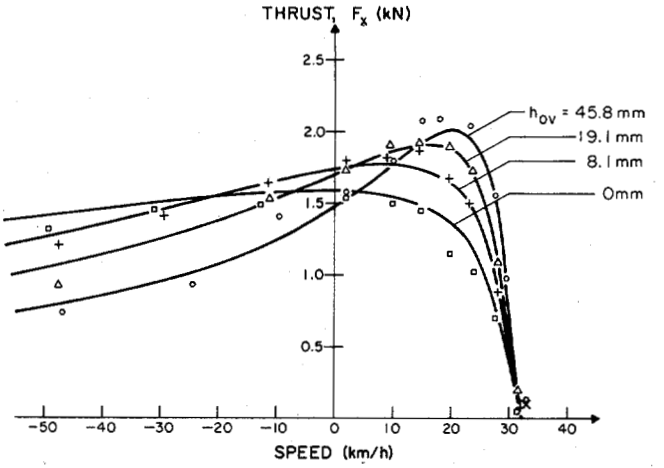

Fig. 6. Influence of aluminum cap overhang (i.e., side-bar width) on thrust, at $I = 200$ A, $f = 18$ Hz, $g = 15$ mm, $d = 2.5$ mm, $w = 111$ mm.

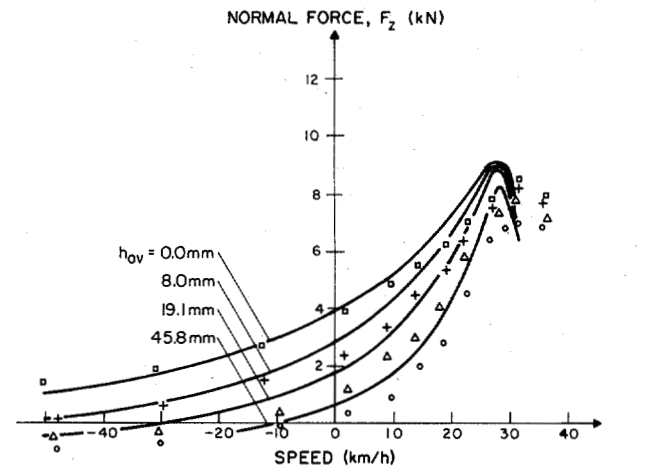

Fig. 7. Influence of aluminum cap overhang (i.e., side-bar width) on normal force, at $I = 200$ A, $f = 18$ Hz, $g = 15$ mm, $d = 2.5$ mm, $w = 111$ mm.

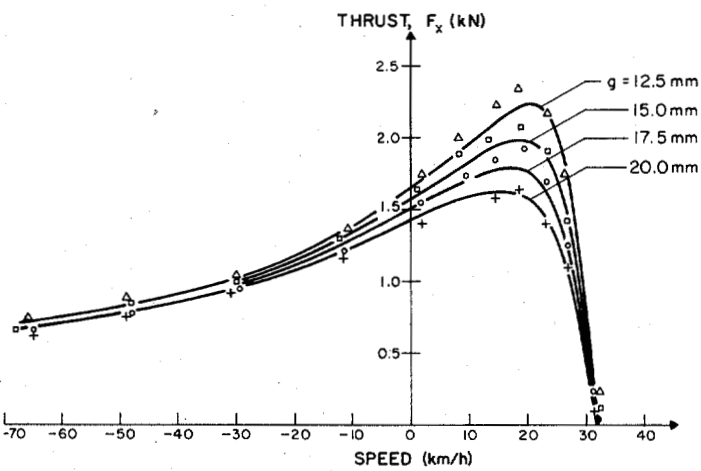

Fig. 8. Thrust F_x as function of speed at various airgaps, for $I = 200$ A, $f = 18$ Hz, $d = 2.5$ mm, $w = 111$ mm, $h_{ov} = 33.9$ mm.

and 9. It may be noted that a LIM with aluminum-capped secondary is less sensitive to variations in airgap than a LIM with solid steel reaction rail [6].

Thrust and normal forces as a function of speed at various levels of constant current in the range $100 < I <$

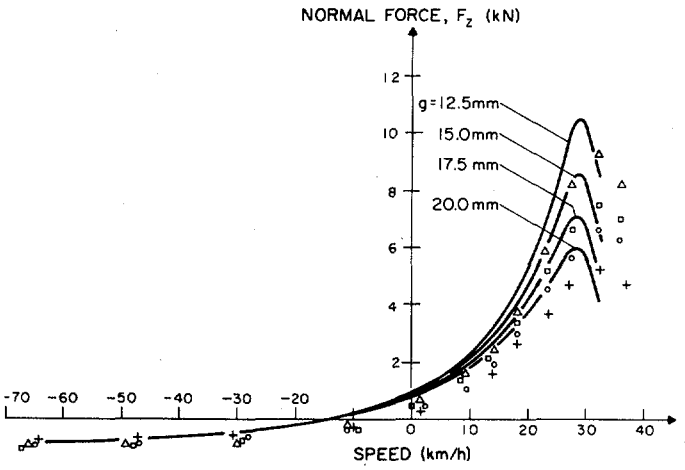

Fig. 9. Normal force F_z as function of speed at various airgaps, for I = 200 A, f = 18 Hz, d = 2.5 mm, w = 111 mm, h_{ov} = 33.9 mm.

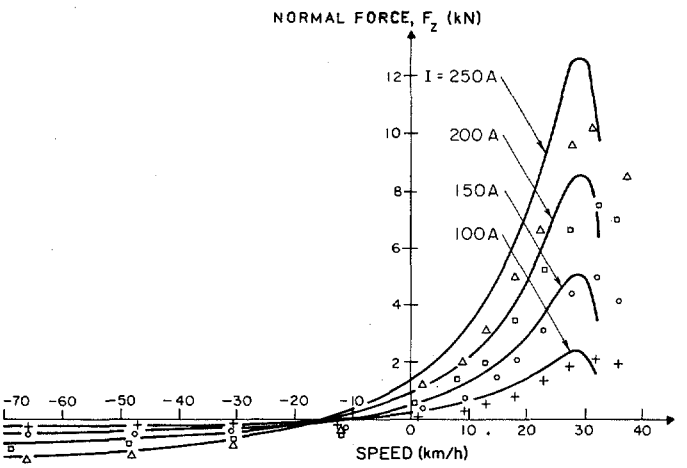

Fig. 11. Normal force F_z as function of speed at constant currents, for f = 18 Hz, g = 15 mm, d = 2.5 mm, w = 111 mm, h_{ov} = 33.9 mm.

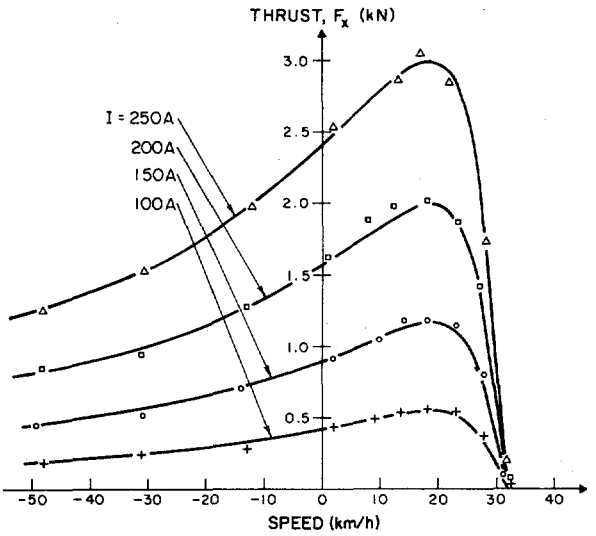

Fig. 10. Thrust F_x as function of speed at constant currents, for f = 18 Hz, g = 15 mm, d = 2.5 mm, w = 111 mm, h_{ov} = 33.9 mm.

250 A are shown in Figs. 10 and 11, for f = 18 Hz, g = 15 mm, h_{ov} = 33.9 mm.

For Figs. 4–11, the thrust and normal force curves were calculated for the fundamental space harmonic $\nu = 1$ using the T-type equivalent circuit shown in Fig. 2, from the analytical expressions (45), (47), (48), and (50). It has been shown that the influence of higher space harmonics on thrust, for slip $s > 0.5$, is very small (see Appendix III).

Conclusion

By comparing the experimental points to the analytical curves in Figs. 4–11, it may be concluded that the method for determining the mechanical performance of a linear induction motor with double-layer secondary as presented in this paper gives very good results over a wide range of frequency, airgap, current, and secondary overhang.

While this analytical approach is based on an equivalent circuit of the LIM, both mutual and secondary impedance have been evaluated from an analysis of the two-dimensional electromagnetic field distribution in the machine. Mutual impedance takes into account the nonlinearity of the magnetic circuit by including a saturation factor (2). Secondary impedance includes both complex permeability of the rail (1), which models field dependent magnetic permeability and hysteresis losses, and transverse edge effects through the correction factor discussed in Appendix II. Longitudinal end effects are included by modifying the EMF across the mutual impedance; this factor being particularly significant when $0 < s < 0.35$.

Under constant current conditions, both the maximum available thrust and the peak normal force are decreased as the input frequency is increased, primarily through the influence of longitudinal end effects and saturation of the magnetic circuit. At a particular frequency, increasing the airgap from 12.5 mm to 20.0 mm decreases the peak thrust and normal force by only about 25 and 50 percent, respectively. In plugging operation ($s > 1$), the thrust and normal forces are even less sensitive to airgap.

The effect of rail cap overhang cross section was investigated by incrementally reducing the width of the aluminum cap. It was shown analytically and experimentally that LIM performance is insensitive to overhang cross section above a certain value. Reducing the overhang below this value produces a decrease in the maximum available thrust and the peak normal force. The overhang dimension below which performance is degraded is considered to be that at which the effective longitudinal resistance of the side bar becomes significant in comparison with the effective transverse resistance of the cap over the core.

The equivalent circuit approach, with mutual and secondary parameters evaluated from two-dimensional field analysis with appropriate correction factors for edge, end and saturation effects, provides an effective tool for the calculation of LIM performance. This technique can be used for design studies of LIM's for transportation applications under constant current or, by including an additional iterative loop in computation, under constant voltage excitation conditions.

APPENDIX I
SATURATION FACTOR OF MAGNETIC CIRCUIT

The saturation factor k_μ of the magnetic circuit is evaluated by relationship (2). Because of the very high magnetic permeability assumed for the primary core, the magnetic potential drop across teeth and yoke of the primary core tends to zero. MMF due to the νth harmonic per pole pair is, therefore, equal to

$$V_\nu \simeq 2|V_{g\nu}| + 2|V_{d\nu}| + |V_{2\nu}| \tag{52}$$

where

1) magnetic potential drop across the airgap is

$$V_{g\nu} = \int_0^{g'} H_{mz\nu 3}\Big|_{x=0} dz = j\left\{\left[(\mu_{re}\cosh(\kappa_{\nu 2}d) + \frac{\kappa_{\nu 1}}{\kappa_{\nu 2}}\sinh(\kappa_{\nu 2}d)\right]\frac{\sinh(\beta_\nu g')}{\beta_\nu} - \frac{\kappa_{\nu 2}}{\beta_\nu}\left[\frac{\kappa_{\nu 1}}{\kappa_{\nu 2}}\cosh(\kappa_{\nu 2}d) + \mu_{re}\sinh(\kappa_{\nu 2}d)\right]\cdot\frac{1-\cosh(\beta_\nu g')}{\beta_\nu}\right\}\frac{A_{m\nu}}{M_\nu}, \tag{53}$$

2) magnetic potential drop across the high conductivity nonmagnetic layer is

$$V_{d\nu} = \int_{g'}^{d+g'} H_{mz\nu 2}\Big|_{x=0} dz = j\left[\mu_{re}\frac{\sinh(\kappa_{\nu 2}d)}{\kappa_{\nu 2}} - \frac{\kappa_{\nu 1}}{\kappa_{\nu 2}}\frac{1-\cosh(\kappa_{\nu 2}d)}{\kappa_{\nu 2}}\right]\frac{A_{m\nu}}{M_\nu}, \tag{54}$$

3) mean magnetic potential drop in the solid steel core in the x direction $V_{2\nu}$ is given in [6]. Equations (53) and (54) should be put into (2) with $\nu = 1$.

APPENDIX II
EDGE EFFECT IN HIGH CONDUCTIVITY NONMAGNETIC LAYER

Edge effect for the high conductivity layer may be taken into account by means of the Russell and Norsworthy [19] factor, i.e.,

$$k_{RN\nu} = 1 - \frac{\tanh\left(\beta_\nu\frac{w}{2}\right)}{\beta_\nu\frac{w}{2}\left[1+\tanh\left(\beta_\nu\frac{w}{2}\right)\tanh(\beta_\nu h_{ov})\right]}. \tag{55}$$

This expression may be applied for space harmonics $\nu > 1$, although Russell and Norsworthy [19] presented it only for the first space harmonic. The coefficient $k_{RN\nu} < 1$ takes into account currents along the x axis and effectively reduces the electric conductivity of the nonmagnetic layer. In practice, the thickness of overhang t_{ov} is usually greater than the thickness of the layer over the solid iron core (Fig. 12). In this case tanh $(\beta_\nu h_{ov})$ should be multiplied by the factor

$$1 + 1.3\frac{t_{ov}-d}{d} > 1. \tag{56}$$

This correction factor (56) has been estimated in an empirical manner.

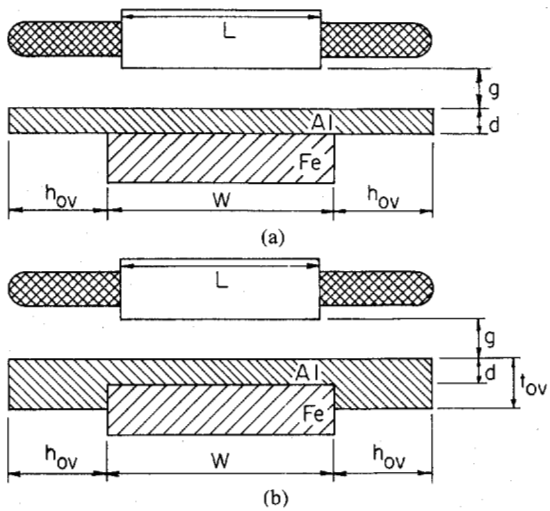

Fig. 12. Double-layer secondary with aluminum cap over solid steel core. (a) Uniform thickness in overhang and over core. (b) Thickness in overhang (side bars) greater than that over core.

TABLE I
INFLUENCE OF SPACE HARMONICS ON THRUST OF THE TEST LIM

ν	$k_{w\nu}$	$\frac{F_{x\nu}}{F_{x\nu}=1}$ [percent] $s = 0.5$	$s = 1.0$
1	0.902	100.0000	100.0000
5	−0.038	−0.0335	−0.0189
7	−0.136	−0.1516	0.0936
11	−0.136	−0.0938	−0.0244
13	−0.038	−0.0038	0.0011
17	0.902	−1.5611	−0.2848
19	−0.902	−0.9926	0.2016
23	0.038	−0.0013	−0.0002
25	0.136	−0.0120	0.0019
	Total	97.1503	99.9699

$s = 1.0$, $f = 18$ Hz, $I = 200$ A, $g = 15$ mm, $d = 2.5$ mm, $w = 111$ mm.

APPENDIX III
INFLUENCE OF HIGHER SPACE HARMONICS ON THRUST

The effect of higher space harmonics on thrust has been determined using the equivalent circuit. The results for the test LIM are given in Table I. While the 17th and 19th harmonics are the most significant, the effect of all higher space harmonics is very small. While small, the influence of higher space harmonics on thrust is greater for a LIM with two layer (aluminum-capped) secondary than for a LIM with a homogeneous solid steel reaction rail [6].

ACKNOWLEDGMENT

One of the authors (J.F.G.) is indebted to NSERC for an International Scientific Exchange Award to conduct research at Queen's University for the year 1983/84.

REFERENCES

[1] E. R. Laithwaite, *Induction Machines for Special Purposes*. London: Newnes, 1966.

[2] S. A. Nasar and I. Boldea, *Linear Motion Electric Machines*. New York: Wiley, 1976.

[3] S. Yamamura, *Theory of Linear Induction Motors*. New York: Wiley, 1972.

[4] M. Poloujadoff, *The Theory of Linear Induction Machinery*. Oxford: Clarendon, 1980.

[5] G. E. Dawson, A. K. Wallace, A. R. Eastham, and A. M. A. Kamar, "Design study of a LIM with solid steel reaction rail for urban transit," in *Proc. Int. Conf. Electrical Machines*, ICEM '82, Budapest, 1982, part 3, pp. 992–995.

[6] J. F. Gieras, A. R. Eastham, and G. E. Dawson, "Performance calculation for single-sided linear induction motors with a solid steel reaction plate under constant current excitation," *Proc. IEE*, Part B, vol. 132, pp. 185–194, 1985.

[7] G. E. Dawson and A. R. Eastham, "The comparative performance of single-sided linear induction motors with squirrel-cage, solid-steel and aluminum-capped reaction rails," in *16th Annu. IEEE Ind. Appl. Soc. Meeting*, Philadelphia, Oct. 1981, IEEE Conf. Record 81 CH 1678-2, pp. 323–329.

[8] A. Smilgevicius, "Impedance of ferromagnetic rotor with conductive cap," (in Russian), in *Elektriceskie Masiny i Elektroprivod Maloj Moscnosti*, Moskva-Leningrad, Nauka, 1960, pp. 90–95.

[9] M. S. Sarma and G. R. Soni, "Solid-rotor and composite-rotor induction machines," *IEEE Trans. Aerospace*, vol. AES-8, pp. 147–155, 1972.

[10] J. Gieras, "Theory of induction machines with double-layer secondary," *Rozprawy Elektrotechniczne*, 23, pp. 577–631, 1977.

[11] E. M. Freeman, "Travelling waves in induction machines: Input impedance and equivalent circuits," *Proc. IEE*, vol. 115, pp. 1772–1776, 1968.

[12] E. M. Freeman and D. A. Lowther, "Normal force in single-sided linear induction motors," *Proc. IEE*, vol. 120, pp. 1499–1506, 1973.

[13] B. T. Ooi and D. C. White, "Traction and normal forces in linear induction motor," *IEEE Trans. Power Apparatus Syst.*, vol. PAS-89, pp. 638–645, 1970.

[14] I. Boldea and M. Babescu, "Multilayer approach to the analysis of single-sided linear induction modors," *Proc. IEE*, vol. 125, pp. 283–287, 1978.

[15] M. Yamazoe, "Analysis and experiments of single-sided linear induction motor," *Elect. Eng. Japan*, vol. 100, pp. 9–18, 1980.

[16] S. Tanaka and S. Tadakuma, "Magnetic levitation and propulsion system by single-sided linear induction motor," *Elect. Eng. Japan*, vol. 100, pp. 116–123, 1980.

[17] M. Ivamoto, S. Sakabe, K. Itani, K. Kitagawa, and G. Utsumi, "Experimental and theoretical study of high speed single-sided linear induction motors," *IEE Proc. Part B, Electric Power Applications*, vol. 128, pp. 306–312, 1981.

[18] J. F. Gieras, "Analytical method of calculating the electromagnetic field and power losses in ferromagnetic halfspace, taking into account saturation and hysteresis," *Proc. IEE*, vol. 127, pp. 1098–1104, 1977.

[19] R. L. Russell and K. M. Norsworthy, "Eddy currents and wall losses in screened rotor induction motors," *Proc. IEE*, vol. 105A, pp. 163–175, 1958.

[20] A. I. Voldek, "Induction magnetohydrodynamic machines with liquid metal secondary" (in Russian), Energia, Leningrad, 1970.

[21] K. Yoshida, "New transfer-matrix threoy of linear induction machines, taking into account longitudinal and transverse ferromagnetic end effects," *IEE Proc., Part B, Electric Power Application*, vol. 128, pp. 225–236, 1981.

[22] T. Hirasa, S. Ishikawa, and T. Yamamuro, "Equivalent circuit of linear induction motors with end effect taken into account," *Elec. Eng. Japan*, vol. 100, pp. 65–71, 1980.

[23] J. Gieras, "Elements of electromagnetic theory of induction machines," (in Polish), D.Sc. thesis, Zeszyty Naukowe ATR *Elektrotechnika*, no. 2, Bydgoszcz, Poland, 1979.

[24] J. F. Gieras, "Simplified theory of double-sided linear induction motor with squirrel-cage secondary," *IEE Proc., Part B*, vol. 130, pp. 424–430, 1983.

[25] A. R. Eastham, G. E. Dawson, D. L. Atherton, and C. L. Schwalm, "Test facility for determination of linear induction motor performance," CIGGT Rep. No. 80-6, Queen's Univ., Kingston, 1980.

[26] A. R. Eastham, G. E. Dawson, D. M. Pringle, and J. M. Davidson, "Comparative experimental evaluation of the performance of a SLIM with a solid-steel reaction rail and with an aluminum-capped reaction rail," CIGGT Rep. No. 80-7, Queen's Univ., Kingston, 1980.

[27] J. F. Gieras, G. E. Dawson, and A. R. Eastham, "A new longitudinal end effect factor for linear induction motors," Paper 86 WM 209-1, presented at IEEE Power Engineering Society 1986 Winter Meeting, New York, Feb. 1986.